Characterization of in-situ ion irradiated Fe-21Cr-32Ni austenitic model alloy and alloy 800H at low doses

M. Ayanoglu*, C.J. Ulmer, A.T. Motta

Ken and Mary Alice Lindquist Department of Nuclear Engineering, The Pennsylvania State University, University Park, PA, 16802, USA

ARTICLE INFO

ABSTRACT

The microstructural evolution of ternary Fe-21Cr-32Ni (21Cr32Ni) model alloy and of alloy 800H was investigated with a series of in-situ ion irradiation experiments performed using the Intermediate Voltage Electron Microscope (IVEM)-Tandem Facility at Argonne National Laboratory (ANL). Samples were irradiated in-situ with 1 MeV Kr^{++} ions in the temperature range of 50K to 713K to doses up to 2 dpa. The size distribution of defect clusters, average defect cluster diameter, and defect cluster density were measured and compared. Results showed that the evolution of defects (i.e. the average defect cluster size and number density) in 21Cr32Ni model alloy and alloy 800H with dose were similar at irradiation temperatures up to 300K where they initially increased with dose up to 0.1 dpa after which no significant changes in defect size and density were observed with further irradiation. In addition, both alloys exhibited ordered defect structures along the <100> direction at relatively low temperatures, up to 300K, which remained stable throughout post-irradiation in-situ thermal annealing up to a temperature of 773K. During irradiation at 713K, small defect clusters were observed at low doses (<0.1 dpa) in both alloys. However, at this irradiation temperature, the clusters in 21Cr32Ni grew with a faster rate than those formed in alloy 800H, causing the microstructure in the former to be dominated by numerous large dislocation loops having both {111}- and {110}-type habit planes, and in the latter to be dominated by small defect clusters and small {111}-type dislocation loops. This may indicate that defect trapping by the solute atoms in alloy 800H at 713K can slow point defect migration to defect clusters and limit their growth.

1. Introduction

Potential improvements of new generation fission and fusion energy systems require the development of new materials and increased understanding of how those materials behave in the reactor core at high doses. In these reactor concepts, the in-core components must withstand radiation damage levels which can reach up to 200 dpa (displacements per atom) at operating temperatures of more than 400°C [1].

Several alloys have been selected as promising candidates to be used as in-core structural materials. Among them, the Fe-Cr-Ni based super alloy 800H has been considered as one of the primary candidate alloys for the construction of the high temperature components (such as fuel cladding, core barrel, core support floor, steam generator, intermediate heat exchangers, hot ducts etc.) in the Gas-cooled Fast Reactor (GFR), Lead-cooled Fast Reactor (LFR), Sodium-cooled Fast Reactor (SFR) and Super-Critical Water Reactors (SCWR) because of its resistance to high temperature corro-

sion and creep [2-3]. Although many studies have been published in the literature on the microstructure evolution of different types of Fe-Cr-Ni austenitic steels when subjected to proton, neutron or heavy-ion irradiations in a wide temperature range (~550 K to ~900 K) [4-18], only a few studies have been conducted specifically on austenitic alloy 800H and the majority of those studies were aimed at determining the effects of high dose levels on the material microstructure [19 22]. Because irradiation-induced features observed at high doses derive from the initial microstructure evolution, the main focus of the present study is on the low dose (up to ~1-2 dpa) behavior of the Fe-based 21Cr32Ni type austenitic alloys; especially the initial defect evolution and how alloying elements may influence this process. It is known that the solute-defect interactions can cause point defects to be trapped by alloying elements in solid solution during irradiation [23,24]. Therefore, alloying elements can influence defect accumulation by acting as effective point defect recombination sites or as effective nucleation sites for larger defect clusters. For example, the doping of Si in Fe-Ni resulted in a significant number of interstitial atoms to be trapped and to form interstitial clusters [23], whereas the addition of Ti or Al in Fe-Ni and Fe-Cr-Ni type alloys resulted in the

Table 1
Bulk chemical composition of major constituents of 21Cr32Ni model alloy and commercial 800H measured by direct current plasma (DCP) method.

Alloy	Fe	Ni	Cr	Mn	Al	Ti	Cu	Si	V	Mo	Others (C*, P*, N, H, O, W, S)
21Cr32Ni	Bal.	31.2	20.7	0.9	–	–	–	0.1	–	0.02	~0.04
800H	Bal.	30.9	20.3	0.74	0.56	0.34	0.36	0.16	0.04	0.07	~0.17

* Combustion method (CO) used for carbon and sulfur measurement.

formation of vacancy clusters [23,24]. It is important to note that because of multiple alloying elements, the overall irradiation behavior of commercial steels is more complex than that of model alloys. For example, Jung et al. reported that the addition of Si and P into the Fe-Cr-Ni-Mo alloy system reduced swelling and creep during irradiation with 6.2 MeV protons at 773K, whereas the addition of C and N resulted in the enhancement of swelling [25]. Interestingly, the swelling strain measured in the commercial 316L-type steel including Ni-Si-P-C-N was the lowest among the alloys in their study. Similarly, Garner et al. studied the behavior of Fe-Cr-Ni type austenitic stainless steels irradiated in the EBR-II in the temperature range of 673K-932K and reported that the addition of Si and P to Fe-Cr-Ni alloys which contains other solutes can increase swelling [26]. All these studies show that the alloying elements strongly influence the radiation damage behavior of Fe-Cr-Ni alloys in many ways.

In this paper, the results of systematic in-situ ion irradiation experiments performed on a 21Cr32Ni austenitic model alloy and on commercial alloy 800H are reported. Electro-polished thin foils of 21Cr32Ni model alloy and alloy 800H were irradiated at the Intermediate Voltage Electron Microscope (IVEM) at Argonne National Laboratory using 1 MeV Kr^{++} ions at irradiation temperatures between 50K and 713K. The initial defect evolution and the defect size distribution and density vs. dose behavior were obtained as a function of irradiation temperature and dose up to ~2 dpa and the results were compared. These results are analyzed to discuss the role of the minor alloying elements in the microstructural evolution of alloy 800H during irradiation.

2. Experiment

2.1. Material and sample preparation

The 21Cr32Ni model alloy used in this study was provided by GE Global Research as heat #RAM-2192, and alloy 800H was provided by GE Carlson Inc. as heat #35175. The elemental compositions of the alloys were measured by Sherry Laboratories and Luvak Inc., respectively using direct current plasma (DCP) emission spectroscopy. The chemical compositions of major constituents in the alloys are shown in Table 1. The grain size of the alloys was determined by optical microscopy to be ~50 μm for 21Cr32Ni and ~200 μm for alloy 800H, after the polished surface was exposed to an etchant having a composition of 10 mL of HNO$_3$, 20 mL of HCl, and 30 mL of H$_2$O.

For phase determination, as-received alloys were sent to the Advanced Photon Source (APS) at Argonne National Laboratory (ANL) for X-ray diffraction (XRD) analysis. The 33-ID-D beamline was used for the measurements, using a beam size of 260 μm×160 μm and 19.9 keV (λ=0.623037 Å) beam energy. The XRD patterns were then analyzed by comparing the peak intensities and the peak positions (2θ values) with the powder diffraction files (PDF) up to 2θ = 40° (corresponding to an atomic plane spacing of ~0.1 nm).

Samples for transmission electron microscopy (TEM) characterization were prepared by cutting 3-mm disks from the bulk material characterization using electrical discharge machine (EDM). These disks were then ground with 600/800/1200 grit paper from both sides to a final thickness of less than ~120 μm followed by electro-polishing using a 95% methanol and 5% perchloric acid solution as the electrolyte. The temperature was always kept below -30°C during electro-polishing by adding liquid nitrogen. Once the polishing step was completed, the sample holder was put into a beaker of methanol for ~1 min to stop further etching. The TEM disks were then removed from the holder and rinsed three times using a sequence of methanol, ethanol, and methanol for ~ 1 min in each.

Fig. 1 shows the microstructure characterization of the as-received steels by XRD and TEM. The XRD patterns in Fig. 1a show that the major phase observed in the alloys before irradiation is the austenitic phase with the corresponding lattice constant of a=3.58 Å, a typical value for fcc-Fe which was verified with the reference PDF data (shown with black markers PDF# 98-000-0258). The normalized intensities of the major peaks are also consistent with the PDF data, although some of the XRD peaks (such as 311 and 222 peaks in Fig. 1a show some slight variation from the values reported in the PDF file. This could be caused by sample texture or because a limited number of grains are probed due to the large grain size. Fig. 1a also shows additional small peaks in the 21Cr32Ni model alloy at relatively low 2θ values. These peaks were compared with possible oxide and carbide/nitride PDF files and they are consistent with small amounts of oxide phases (Fe$_3$O$_4$ and Cr$_2$O$_3$ type), shown in green which may have formed on the surface from exposure to air. Fig. 1 (b-c) show that the 21Cr32Ni model alloy and alloy 800H have a similar pre-existing dislocation microstructure. The dislocation structure in the grains were homogenous. There were some slight variations in the grain-to-grain dislocation density. The line dislocation density in both alloys was calculated to fall in the range of 10^{14}-10^{15} m^{-2}.

2.2. IVEM experiments

In-situ ion irradiation experiments were performed at the Argonne National Laboratory (ANL) Intermediate Voltage Electron Microscope (IVEM). This is a Hitachi-9000 transmission electron microscope having a side entry stage and operated at 200 keV. Samples were irradiated using 1 MeV Kr^{++} ions with an ion flux of 2.84×10^{11} ions/cm^2-s at temperatures ranging from 50K to 713K. The ion energy was selected so that the Kr ions traversed the sample rather than being implanted. The ion range and displacement damage were calculated using the Stopping and Range of Ion in Matters (SRIM) software. The ion range was ~300 nm, i.e., approximately three times larger than a typical ~100 nm thick electron transparent TEM sample. Fig. 2a shows the fraction of incident Kr ions passing through a typical ~100 nm thick 21Cr32Ni TEM foil as a function of Kr ion energy. At 1 MeV, ~96% of incident Kr ions pass through the sample. The SRIM damage and ion implantation profiles produced by 1 MeV Kr ion of a typical ~100 nm 21Cr32Ni TEM foil are presented in Fig. 2b which shows a relatively uniform damage profile. The maximum implanted Kr ion concentration in the foil was ~0.007 at.% per dpa.

The sample temperature was continuously monitored throughout the experiments using a thermocouple attached to the specimen cup. Temperature fluctuations during the irradiation were kept within ±5 K. The irradiation was paused at specific doses to
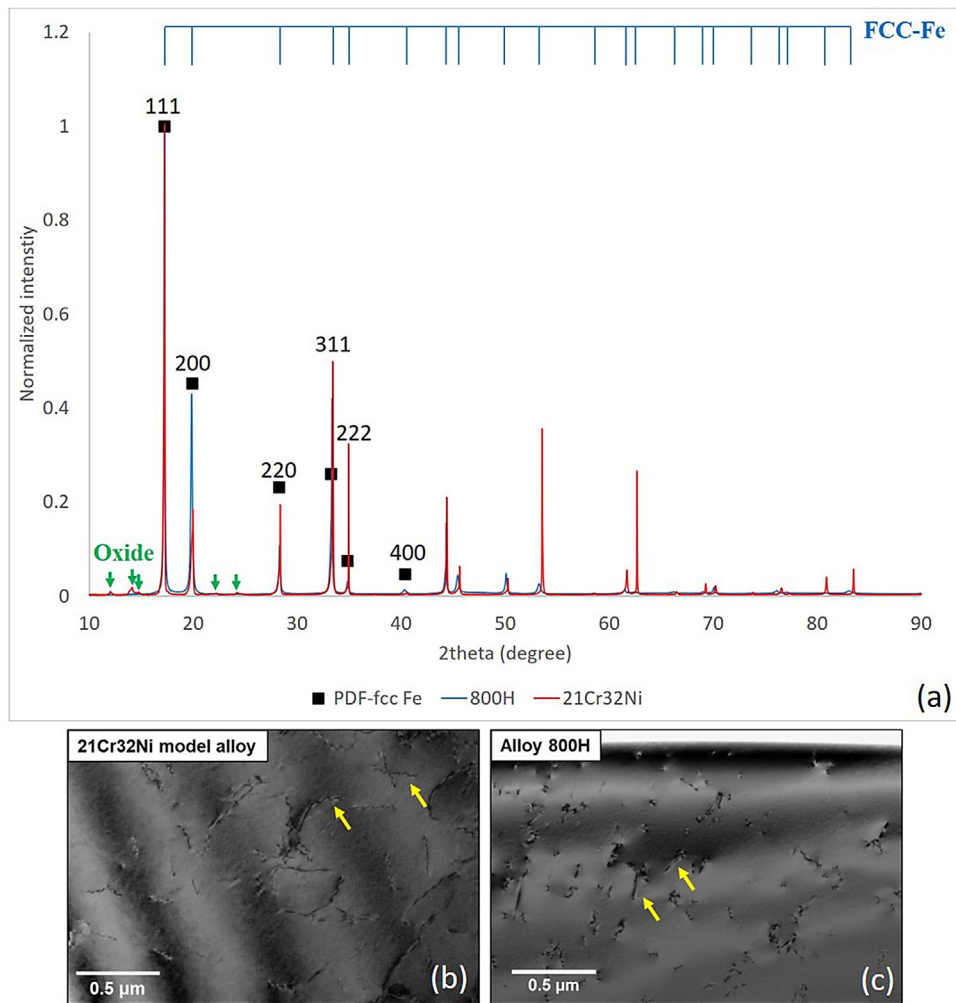
Fig. 1. **(a)** Advanced Photon Source X-ray diffraction patterns acquired from the as-received 21Cr32Ni model alloy (red) and alloy 800H (blue). The intensity on the y-axis is normalized to the maximum peak intensity (i.e. {111} peak). Reference data from powder diffraction file (PDF) up to $2\theta=40°$ is shown with square markers and it shows that main peaks are consistent with fcc-fe. Arrows show additional oxide peaks in the model alloy. **(b-c)** Bright-field TEM images showing the non-irradiated microstructures of 21Cr32Ni model alloy and alloy 800H. Some of the pre-existing dislocations are shown with arrows.
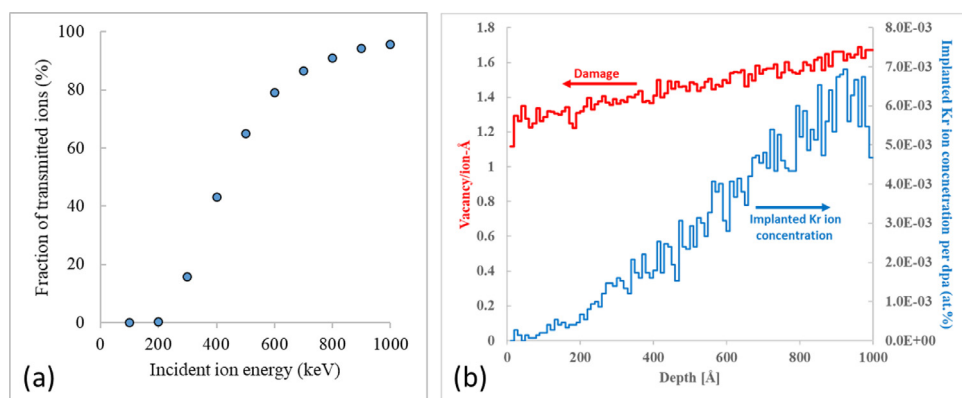
Fig. 2. SRIM simulation results showing (a) the fraction of transmitted Kr ions through a typical ~100 nm thick 21Cr32Ni TEM foil and (b) the damage profile (red) and ion implantation profile (blue) of 1 MeV Kr^{2+} in 21Cr32Ni alloy.

adjust microscope settings and to record images. A systematic effort was spent on selecting a region for tracking that was far from any pre-existing dislocations or grain boundaries. As possible, the TEM images were recorded from the same regions throughout each experiment for consistency.

Table 2 summarizes the irradiation parameters and imaging conditions used in the IVEM experiments. The damage was calculated using SRIM software with the Quick Kinchin-Pease Model and a displacement energy of 40 eV as described in [17,27].

Table 2
Summary of in-situ irradiation conditions and imaging condition for experiment conducted at IVEM on the 21Cr32Ni model alloy.

Temperature[K]	Ion energy and type	Dose rate[dpa/s]	21Cr32Ni	800H
			g-vector	
50	1 MeV Kr^{++}	1×10^{-3}	g_{200}	g_{111}
300			g_{200}	g_{220}
713			g_{200}	g_{200}

Table 3
Deviation parameter, s_g, and effective extinction distance, ξ_{eff}, calculated for different (g, ng) reflections using g_{200}, g_{111} and g_{220} diffraction vectors. The extinction distances, ξ_g, were calculated for fcc-Fe.

g-vector	ξ_g[nm]	(g, ng)	s_g[nm^{-1}]	ξ_{eff} [nm]
{200}	41.6	(g, g)	0.00	41.6
		(g, 2g)	0.04	21.8
		(g, 3g)	0.08	12.3
		(g, 4g)	0.12	8.4
{111}	39.3	(g, g)	0.00	39.3
		(g, 2g)	0.03	25.8
		(g, 3g)	0.06	15.7
		(g, 4g)	0.09	11.0
{220}	52.0	(g, g)	0.00	52.0
		(g, 2g)	0.08	12.5
		(g, 3g)	0.16	6.4
		(g, 4g)	0.23	4.3

Table 4
Average thicknesses of the characterized regions calculated by thickness fringes.

| Temperature[K]	Ion energy/type	Fe21Cr32Ni	800H
		Average thickness [nm]	
50	1	~42 ± 9	~105 ± 11
300	MeV	~129 ± 9	~122 ± 6
713	Kr^{++}	~82 ± 9	~98 ± 9

Table 5
The fraction of loops visible in TEM images recorded using different g-vectors according to the 'g.b' invisibility criteria

loop b-vector [hkl]	g-vector			
	(220)	(111)	(200)	(311)
111	√	√	√	√
1$\bar{1}$1	0	√	√	√
11$\bar{1}$	0	√	√	√
111$^-$	√	√	√	√
110	√	√	√	√
101	√	√	√	√
011	√	√	0	√
1$\bar{1}$0	0	0	√	√
1$\bar{0}$1	√	0	√	√
01$\bar{1}$	√	0	0	0
Visible {111} loop fraction (%)	50	100	100	100
Visible {110} loop fraction (%)	83	50	67	83
Total visible loop fraction (%)	70	70	80	90

2.3. Thickness measurement

To accurately determine defect cluster density, it is essential to have an accurate estimate of the sample thickness, so we spent effort to measure this parameter. The thickness of each sample was determined by counting the thickness fringes which were visible in the bright-field (BF)/dark-field(DF) images recorded at room temperature before irradiation. For thickness determination by thickness fringes, the total number of fringes was multiplied by the effective extinction distance (ξ_{eff}) [28].

The sample thickness was calculated primarily using DF TEM images. If the thickness fringes were also visible in BF TEM images, these were also used, and the sample thickness calculated from both BF and DF images were averaged and reported. The sample thicknesses were measured using the g_{200} diffraction vector with (g, 4g) condition near the [011] zone axis, and the error in thickness measurement was taken as $\pm\xi_{eff}$. Note that different (g, ng) reflections can also be excited in the microscope and used for the thickness determination if ξ_{eff} is calculated for each set of diffraction conditions. Table 3 shows the calculated deviation parameter (s_g) and the effective extinction distance (ξ_{eff}) for various (g, ng) conditions using g_{200}, g_{111} and g_{220} diffraction vectors using fcc-Fe as reference. Table 4 shows the estimated thickness of each of the examined regions in the different samples, calculated using thickness fringes.

2.4. Characterization of the in-situ ion irradiated microstructures

Radiation damage was mainly characterized by analyzing radiation-induced defects and dislocation loops. Defects were counted and their sizes were measured using the ImageJ software [29]. Defect clusters and dislocation loops were counted all together in dark-field images. For consistency, an effort was made to perform defect counting from TEM images recorded using the same magnification (30,000x) and similar deviation parameter. However, higher magnifications were occasionally used to obtain better conditions for defect counting and size measurement, as necessary. The habit planes of the dislocation loops were determined by analyzing bright-field/dark-field TEM images and corresponding diffraction patterns. Imaged loops were identified by comparing the expected projection of circular loops onto the image plane.

For 21Cr32Ni model alloy, DF TEM images were all recorded using the g_{200} diffraction vector with (g, 4g) condition near the [011] zone axis. For alloy 800H, different diffraction vectors with similar deviation parameters were used to optimize defect imaging. The diffraction conditions used in alloy 800H irradiation experiments are g_{111}, g_{220} and g_{200} for 50K, 300K and 713K, respectively. Because most of the defects at the doses of interest (<1 dpa) consists of small defect clusters and dislocation loops, the average defect diameter is not expected to be significantly affected by the change in diffraction conditions since similar deviation parameters were used. On the other hand, the number density of small loops can be affected, as the diffraction conditions change according to "g.b" criteria [28]. Therefore, to be able to compare the defect density as consistently as possible, the number density of the defects was corrected using the "g.b" invisibility criteria. In this approach, all small defects were assumed to be small dislocation loops with Burgers vectors of either {111} or {110}, a logical assumption for the fcc-crystal structure. From this assumption, the fraction of visible loops can be estimated by applying the "g.b" criteria for all possible {111} and {110} type loops, as shown in Table 5. For example, if the g_{220} condition is used for imaging, the fraction of the loops visible in the TEM image is found to be 70% since 3 out of 10 loops are invisible according to "g.b" analysis. In other words, using the g_{220} imaging condition, the loops counted in the TEM image represent about 70% of the total loops present.

The average defect diameter, size distributions, and densities as well as the corresponding errors were then determined with re-
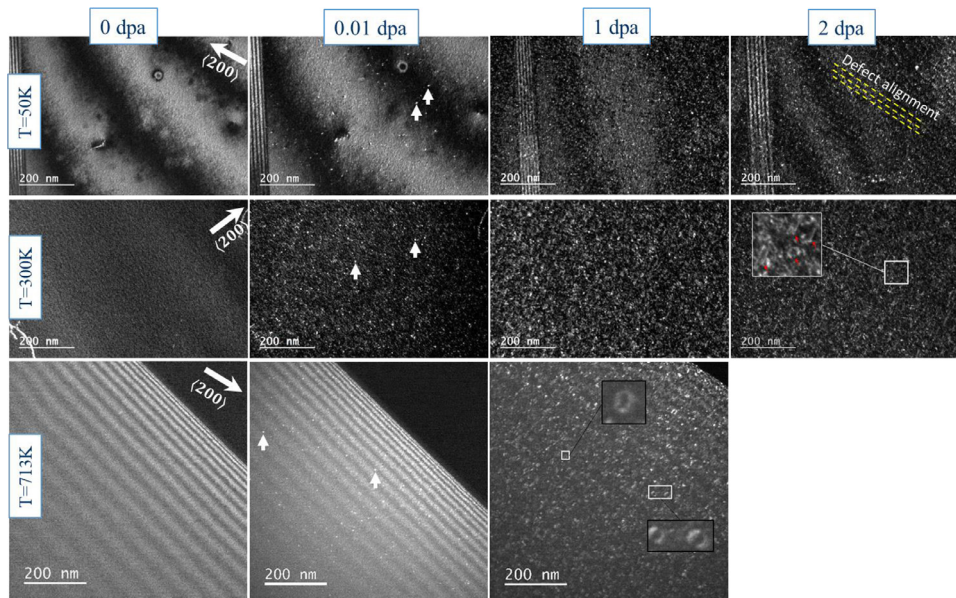
Fig. 3. Dark field transmission electron micrographs showing microstructural evolution of 21Cr32Ni model alloy with dose in dpa for 1 MeV Kr^{2+} irradiation at 50K, 300K and 713K.

spect to irradiation dose, as a function of temperature following the approach given in Ref. [19,21].

3. Results

The main features observed during irradiation of the 21Cr32Ni model alloy and alloy 800H are small defect clusters and dislocation loops. After in-situ irradiation to low doses (~2 dpa), neither 21Cr32Ni model alloy nor the analogous alloy 800H showed any indication of void formation and thus void swelling within the temperature range of 50K-713K. Additionally, based on the diffraction patterns analyzed, no precipitation of new phases occurred during irradiation. Further, once the irradiation was paused, radiation-induced defect formation immediately stopped and the existing small defect clusters were frozen, indicating that little defect formation or migration occurs outside ion irradiation. The following sections present the details of findings observed during in-situ irradiation of the 21Cr32Ni model alloy and commercial alloy 800H.

3.1. Microstructural evolution of the 21Cr32Ni model alloy irradiated at 50K-713K

Fig. 3 shows a sequence of micrographs illustrating the microstructural evolution of 21Cr32Ni model alloy during in-situ irradiation at 50K, 300K and 713K up to ~1-2 dpa. Fig. 4 shows the corresponding average defect cluster diameters and number densities measured from these DF TEM micrographs.

The radiation-induced damage between 50K-713K was first observed at a dose of ~0.005 dpa with the appearance of small white-dots in DF images ("black-dot" damage in BF images) having a diameter of ~2-3 nm. Some of these defects are indicated with arrows in Fig. 3. Because these defects were quite small, their nature could not be identified.
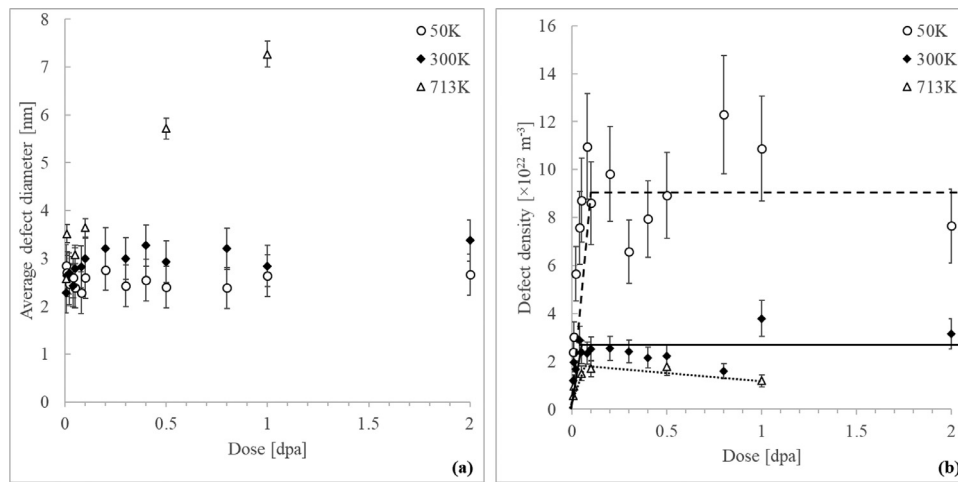
At 50K, radiation-induced defect number density in 21Cr32Ni model alloy quickly increased and saturated at a dose of ~0.1 dpa above which that is no significant change in defect density was observed (see the DF TEM images given in Fig. 3 and also calculated number density vs. dose plot given in Fig. 4). This is a dynamic equilibrium where some defect clusters may disappear while others take their place, i.e., defects continued to appear and disap-

pear with the same rate with further irradiation but caused no net change in density. The measured average defect diameter also remained unchanged throughout the irradiation at 50K as seen in Fig. 4.

The majority of the visible defect clusters were immobile. However, there were a few visible defects which were observed to move during irradiation of the model alloy at 50K (no defect motion was observed when only the electron beam was incident on the sample) as early as ~0.05 dpa. Because these defect clusters may contain many atoms (at least ~100), their mobility is likely driven by loop gliding under irradiation, rather than by thermal diffusion. In agreement with this picture, the observed defect movement was one-dimensional and observed to be slow and continuous, rather than sudden and jerky as was observed in ferritic–martensitic NF616 [30]. Fig. 5a shows video frames which capture the migration of a 4-nm diameter irradiation-induced defect during irradiation. Fig. 5b shows the corresponding diffraction pattern. The direction of the movement was found to be consistent with <110>, as shown in Fig. 5c, which is the nearest neighbor direction in fcc-crystals.

Further irradiation of 21Cr32Ni model alloy to 2 dpa at 50K resulted in an alignment of the small defect clusters. The alignment direction was consistent with the <100> direction, like the previously reported alignment of defect clusters seen in fcc copper and nickel under neutron and ion irradiation to similar doses at temperatures between 370K-570K [31-34]. The direction of the alignment was verified with the DF TEM micrographs recorded using different diffraction vectors as shown in Fig. 6 where it was observed to be unchanged by foil tilting.

The in-situ irradiation of 21Cr32Ni model alloy at 300K was very similar to those observed during irradiation at 50K where small defect clusters (~2-3 nm in size) initially formed, and their density increased and quickly saturated at a dose around ~0.1 dpa (Fig. 4). The saturation of defect cluster number density can be attributed to displacement cascade overlap and annihilation with preexisting clusters formed earlier in the irradiation. Further irradiation of the sample (>0.5 dpa) caused some of the small black-dot type defects to grow by absorbing small invisible defects and caused defect clusters to become dislocation loops. Some of these dislocation loops observed as edge-on at 300K are highlighted with

Fig. 4. (a) Average defect diameter, and (b) defect number density measured for each dose during in-situ irradiations of 21Cr32Ni model alloy at 50K, 300K, and 713K. The irradiation at highest irradiation temperature, 713K, results in larger defects with lower density. (The large error bars in the 50K data are caused by excessive sample bending during irradiation at this temperature which changed the local diffraction conditions and defect counting)
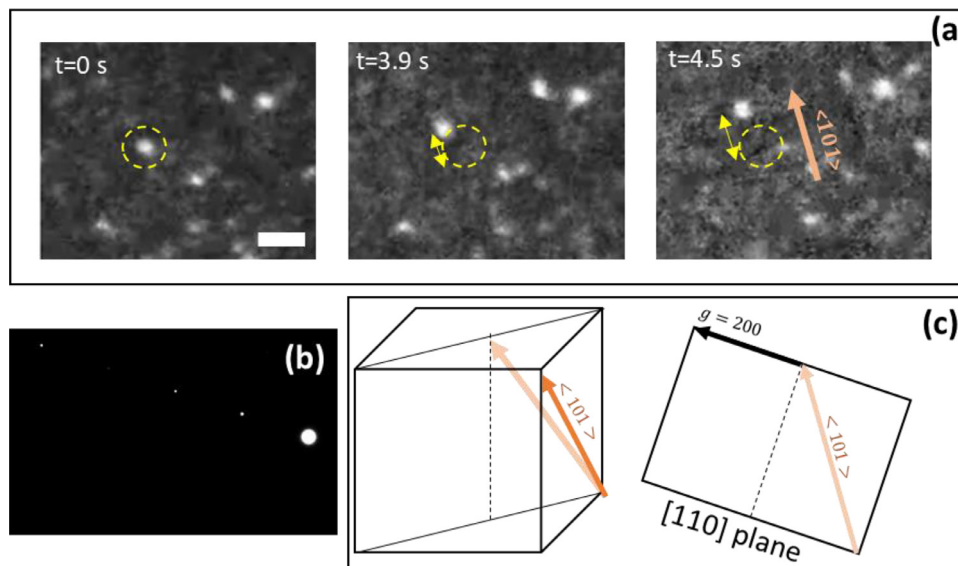
Fig. 5. (a) Dark field images showing the defect migration along <101> direction in 21Cr32Ni model alloy at 50K during the in-situ irradiation with 1 MeV Kr++. Initial position of the defect and the migration direction are highlighted. Scale bar=10 nm. (b) Corresponding diffraction pattern (c) Projection of the <110> directions on the [110] plane.

red arrows in Fig. 3. The habit planes of the edge-on loops at 300K were determined to be mainly {111}-type. The average defect cluster diameter after saturation at 300K was found to be slightly larger than that measured at 50K due to the presence of these relatively large defect clusters and small dislocation loops having ~5-6 nm in size. However, the number density of these loops was very low compared to that of small defect clusters, so that only a little increase in the average defect size was observed, as shown in Fig. 4.

Fig. 3 shows that at low doses (<0.1 dpa), the microstructure of 21Cr32Ni model alloy after irradiation at 713K is similar to that observed at 50K and 300K, i.e. it consisted of ~2-3 nm sized small defects. Thus, the corresponding average defect diameter below ~0.1 dpa at 713K was similar to that observed in the lower temperature irradiations, as shown in Fig. 4. However, these small defect clusters were observed to grow faster during irradiation at 713K than at 300K. The 21Cr32Ni microstructure after irradiation to 0.5 dpa included the formation of small resolvable dislocation loops. Further irradiation of the alloy to ~1 dpa at 713K resulted in more

numerous and larger resolvable dislocation loops than those seen after 300K irradiation to 1 dpa. Also at this high temperature, adjacent growing dislocation loops were observed to coalesce to form larger loops, which was not observed at 300K. Fig. 7 shows a series of BF TEM images that captures a loop coalescence of two adjacent dislocation loops during in-situ irradiation of 21Cr32Ni model alloy between ~0.7 and ~0.82 dpa at 713K, as marked. The loops marked as 'a' and 'b' initially grew, possibly by absorbing small invisible defects or defect clusters which are formed in a nearby cascade, and later coalesced to form the larger loop 'c'.

The formation of numerous large dislocation loops and consequently their coalescence resulted in a pronounced increase in the average defect diameter with no saturation and defect number density to decrease as shown in Fig. 4.

The loops formed under in-situ irradiation of the 21Cr32Ni model alloy at 713K are determined to have both {111}- and {110}-type habit planes, unlike what was observed at 300K. It is known that {111}-type loops are generally observed during irradiation in fcc crystal structure –often faulted in nature-, because the {111}
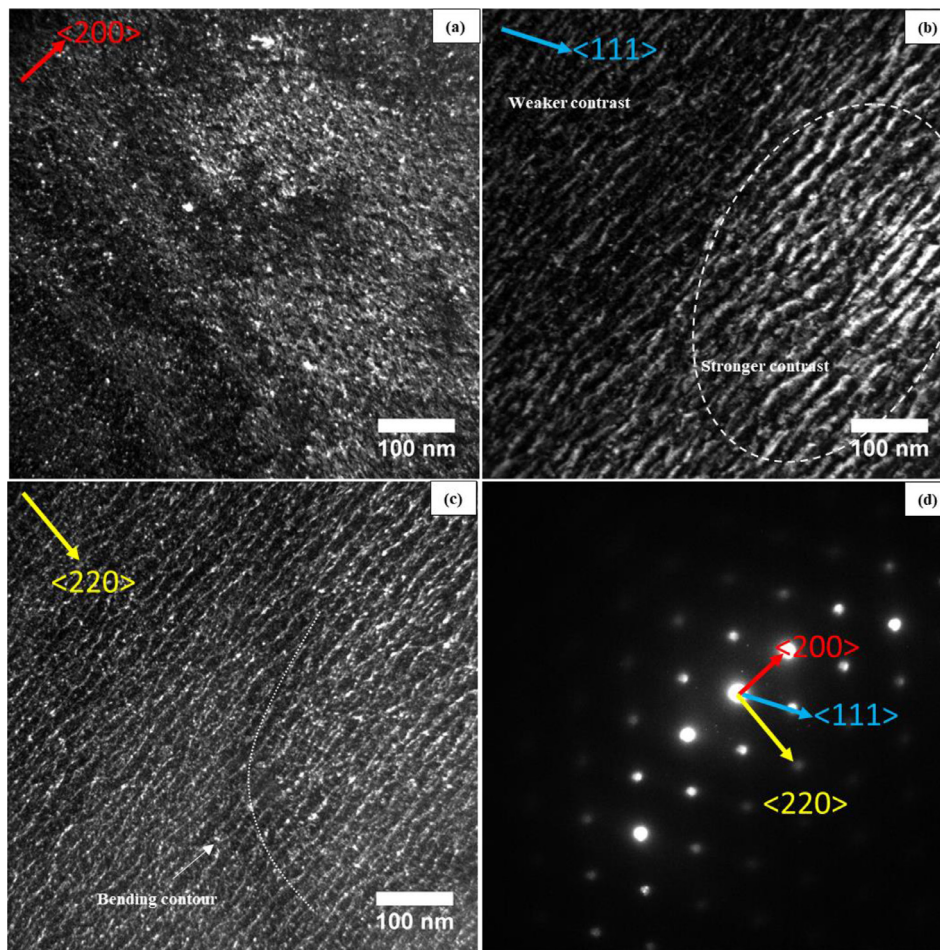
Fig. 6. (a–c) Dark-field TEM images recorded from 21Cr32Ni in-situ irradiated microstructure at 50K to 2 dpa using (a) g_{200}, (b) g_{111}, (c) g_{220}. All diffraction conditions were adjusted near the [110] zone axis as shown in (d). The image given in (b) also shows stronger/weaker contrast of defect segments in certain regions due to sample bending. The bending contours were highlighted with dashed lines shown in (c).

plane is the closed pack plane. It is thought that {110}-type loops at 713K may be formed as a result of the unfaulting of {111}-type faulted loops as a result of the interaction of a nearby growing loop [19,21,35,36].

Finally, the foil thickness was found to influence the microstructural evolution under irradiation such that the thinnest regions of the foils showed little visible damage, likely because of defect elimination at the free surface. Fig. 8 shows a nearby defect-free region near the foil edge (see red box) after irradiation to 1 dpa at 713K as an example.

3.2. Microstructural evolution of alloy 800H in comparison with the 21Cr32Ni model alloy

A series of DF TEM micrographs is presented in Fig. 9 to show the alloy 800H microstructures after in-situ irradiation under similar conditions to that used for 21Cr32Ni model alloy as given previously in Fig. 3. Note that the DF TEM images in this figure was inverted for better defect visibility.

Fig. 9 shows that the microstructure evolution of the commercial alloy 800H between 50K-300K up to ~1 dpa is similar to that of 21Cr32Ni model alloy by which that both microstructures consist of radiation-induced small defect clusters (~2-3 nm in diameter) which increase in number density with dose until saturation. In addition, the irradiation of alloy 800H to ~1 dpa also resulted in defect cluster alignment in the <100> direction similar to what was observed in the 21Cr32Ni model alloy. To determine the

nature of the ordered dislocation structure, additional microscopy was performed. For this purpose, the irradiated alloy 800H sample was systematically tilted and imaged using different diffraction vectors to apply the "g.b" invisibility criteria so that the Burgers vector can be determined. Fig. 10 shows a series of TEM images recorded using different diffraction vectors. The figure shows that the aligned defect structures are only invisible if the diffraction vectors are selected as $g=00\bar{2}$ and $g=\bar{1}\bar{1}3$ which indicates that the Burgers vector direction of aligned structures is $[\bar{1}10]$.

At 713K, irradiation-induced dislocation loops were also observed in the alloy 800H microstructure. Some of these loops are highlighted in Fig. 9. The habit planes of the edge-on loops observed in alloy 800H after 1 dpa irradiation were consistent with {111}-type, similar to what was observed in the 21Cr32Ni model alloy. However, there were no {110}-type dislocation loops detected in the 1 dpa irradiated microstructure of alloy 800H at 713K unlike those seen in 21Cr32Ni model alloy microstructure irradiated under similar conditions. The absence of {110} loops in the alloy 800H might be due to the lower unfaulting rate in alloy 800H than 21Cr32Ni model alloy [19]. The dislocation loops in the 21Cr32Ni after 1 dpa irradiation at 713K were larger than those seen in alloy 800H microstructure.

To investigate the effects of alloying elements on defect size and defect density in alloy 800H, defects formed in alloy 800H were counted and measured in the same way as was done for the model alloy. However, defect counting was only performed for the irradiation temperatures of 300K (up to 0.5 dpa) and 713K where de-
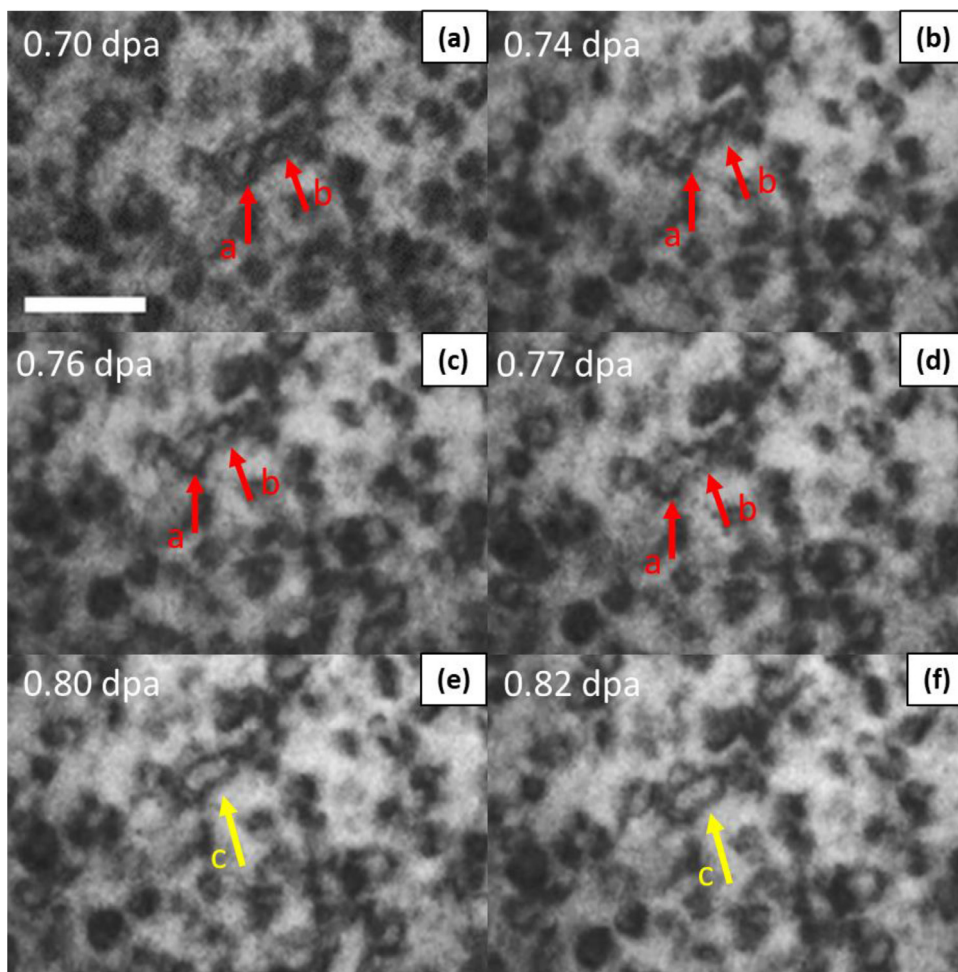
Fig. 7. Bright-field TEM images showing loop coalescence observed during the in-situ irradiation of 21Cr32Ni model alloy at 713K. The images given from (a) to (c) shows the growth of loops 'a" and 'b' by absorbing small invisible defects and defect clusters and coalesce to form loop 'c'. The damage rate used in the experiment is ~1×10^{-3} dpa/s, and the total time for complete coalescence of 'a' and 'b' is ~120 seconds.
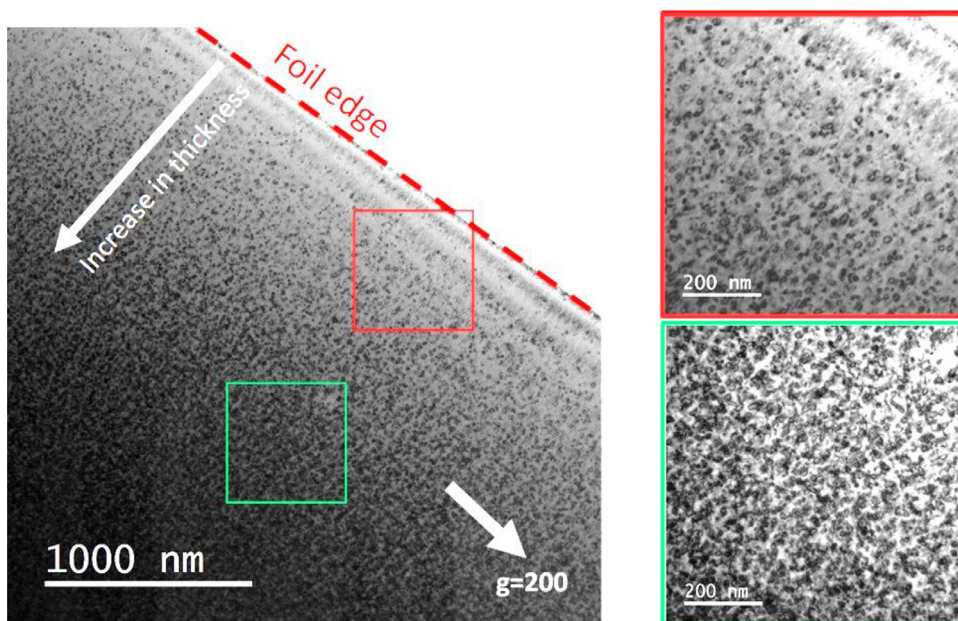

Fig. 8. Bright field TEM images showing the irradiated microstructure after a dose of 1 dpa at 713K. A defect denuded zone is clearly visible near the foil edge.
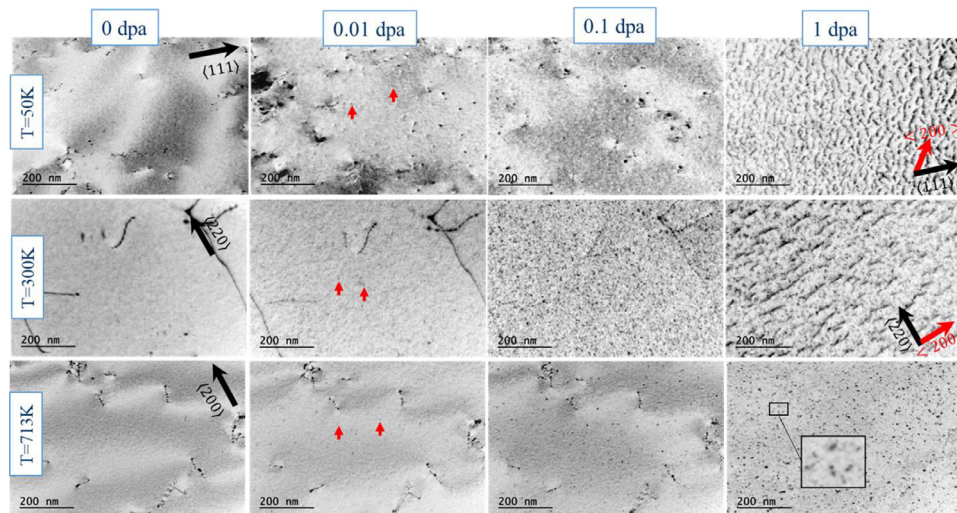
Fig. 9. Dark-field TEM micrographs showing the microstructure of alloy 800H during the in-situ irradiation at 50K, 300K and 713K after specified doses in dpa (Images were obtained in dark-field mode and inverted for better visibility). Radiation-induced small defect clusters are highlighted with red arrows. The diffraction conditions used for imaging are shown with the black arrows given at the top right corner on the first column. The defect alignment along <100> direction was also seen in alloy 800H at a dose of ~1 dpa.
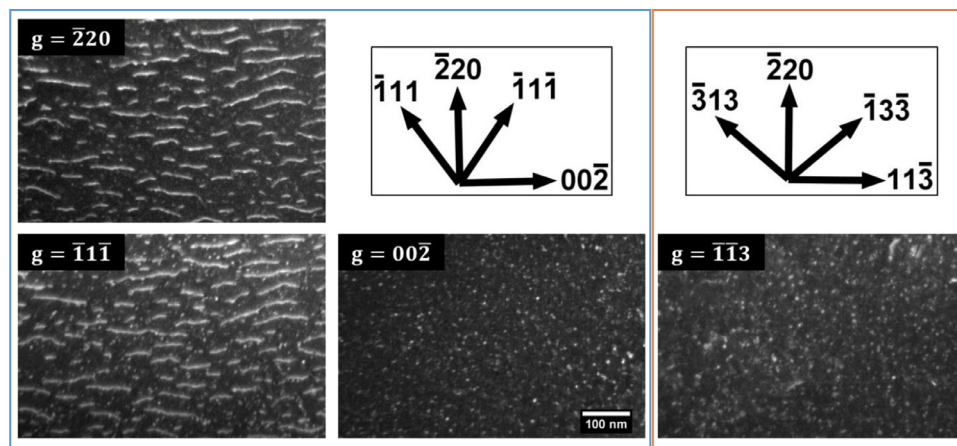
Fig. 10. Dark-field images recorded by using the different diffraction vectors indicated that the Burgers vector direction of the ordered defect structures is consistent with [$\bar{2}20$] according to g.b invisibility criteria.

fect clusters were clearly visible and distinguishable from the background. Only individual defect clusters including dislocation loops were measured and counted as before. The aligned defect structures were excluded from the counting measurement.

Fig. 11 shows a comparison of the defect cluster number density and average diameter calculated after irradiation to successive representative doses up to 1 dpa at 300K and 713K. The figure shows that both the irradiation induced defect cluster size and the defect cluster number density in 21Cr32Ni model alloy at 300K are similar to those determined in alloy 800H as shown in Fig. 11(a-b). In both alloys, the average defect cluster diameter does not change significantly with dose. Whereas, the defect density increases with dose, saturating at about ~0.1 dpa for both alloys. At 713K, however, the average defect size in 21Cr32Ni model alloy increases with dose after ~0.5 dpa due to the formation of numerous large dislocation loops that grow and coalesce with increasing dose. However, the majority of the defects formed in alloy 800H remained as small individual defect clusters. Fig. 11c shows that the defect cluster densities in 21Cr32Ni model alloy and alloy 800H at 713K are similar up to a dose of ~0.1 dpa. However, further irradiation at 713K caused defect cluster number density

to decrease in 21Cr32Ni model alloy due to faster loop growth at that temperature.

4. Discussion

The fact that this study was conducted in-situ allowed us to make unique observations and derive new inferences about the evolution of microstructure during irradiation. Being able to track defect evolution while it is taking place allows us to infer the mechanisms through which it occurs (in terms of defect cluster evolution) to result in the final observed microstructure normally seen after irradiation.

The minimum size TEM-visible defect clusters contain about 100 atoms [30]. As irradiation starts, visible defect clusters appear almost immediately after the start of irradiation - at a dose less than 0.005 dpa. Because very small defect clusters are not visible, it is assumed that the slow accretion of these smaller defect clusters eventually results in the appearance of the large clusters which are visible. However, because the visible defects appear into visibility from one frame to the next, we infer that the occurrence of displacement cascades crates higher order clusters which react with the existing microstructure to form the visible clusters.
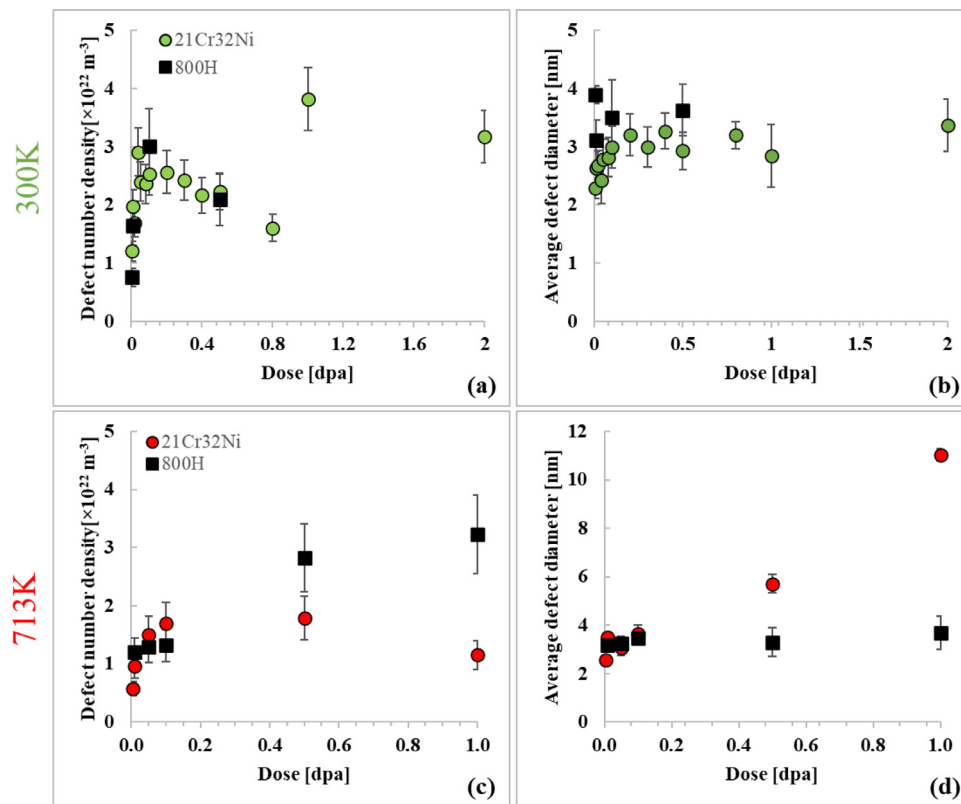
Fig. 11. Plots showing the comparison of the number density and average diameter of defects formed during in-situ irradiation of 21Cr32Ni model alloy and alloy 800H at (a-b) 300K and (c-d) 713K, respectively.
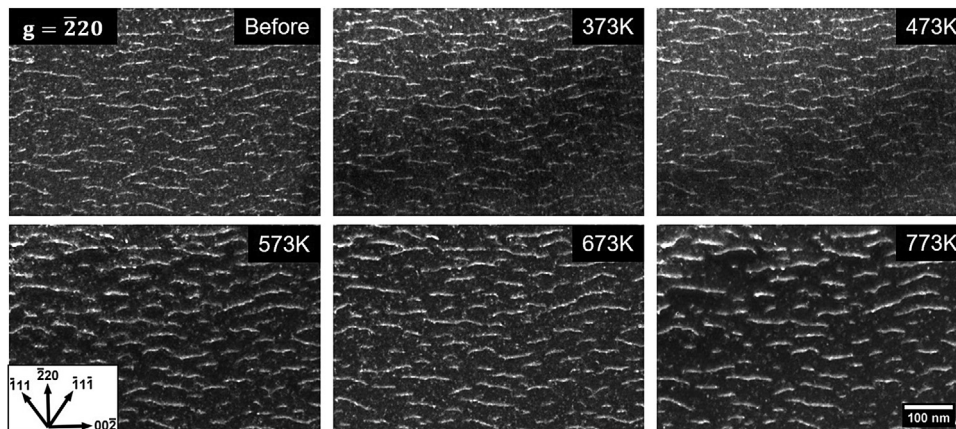
Fig. 12. Dark-field images showing the behavior of the ordered microstructure in alloy 800H during post-irradiation annealing. The ordered defect microstructure formed at room temperature (shown in top-left) remains stable upto 773K.

Given the frame speed in the TEM, we cannot speculate whether the damage seen is created during cascade evolution or whether it occurs in its immediate aftermath, - only that it is not present in one frame and present in the next. Yet, this observation makes it possible to discount processes whereby gradual accretion of point defects over a longer time period would cause cluster formation.

Once the visible defect clusters are formed, it is found that, re-gardless of the irradiation temperature the visible clusters are not mobile, contrary to what was seen in ferritic steels [30,37] but sim-ilar to what was observed during the irradiation of the austenitic steel 800H [21]. On the other hand, the clusters can disappear dur-ing irradiation while other clusters appear. This is also likely due to destruction of clusters by cascade impact as their disappearance is noted from one frame to the next. The creation and destruction

of visible clusters by displacement cascades after a dose of 0.1 dpa gives rise to a dynamic equilibrium, in which the concentration of visible defects remains constant with some defects appearing and others disappearing during irradiation.

Another aspect of microstructure evolution under irradiation that can be explained by observations performed while irradiating in situ is the reduction in size of faulted loops observed at higher doses [19,21]. The reason for this apparent reduction is the unfault-ing of the larger loops by reaction with dislocations under irradi-ation. One of these reactions was observed as it occurred [19] and explains why larger faulted loops are no longer visible using our DF rel-rod imaging technique at higher doses.

The fact that a population of larger loops can be observed after a high enough dose can also be explained based on the observa-
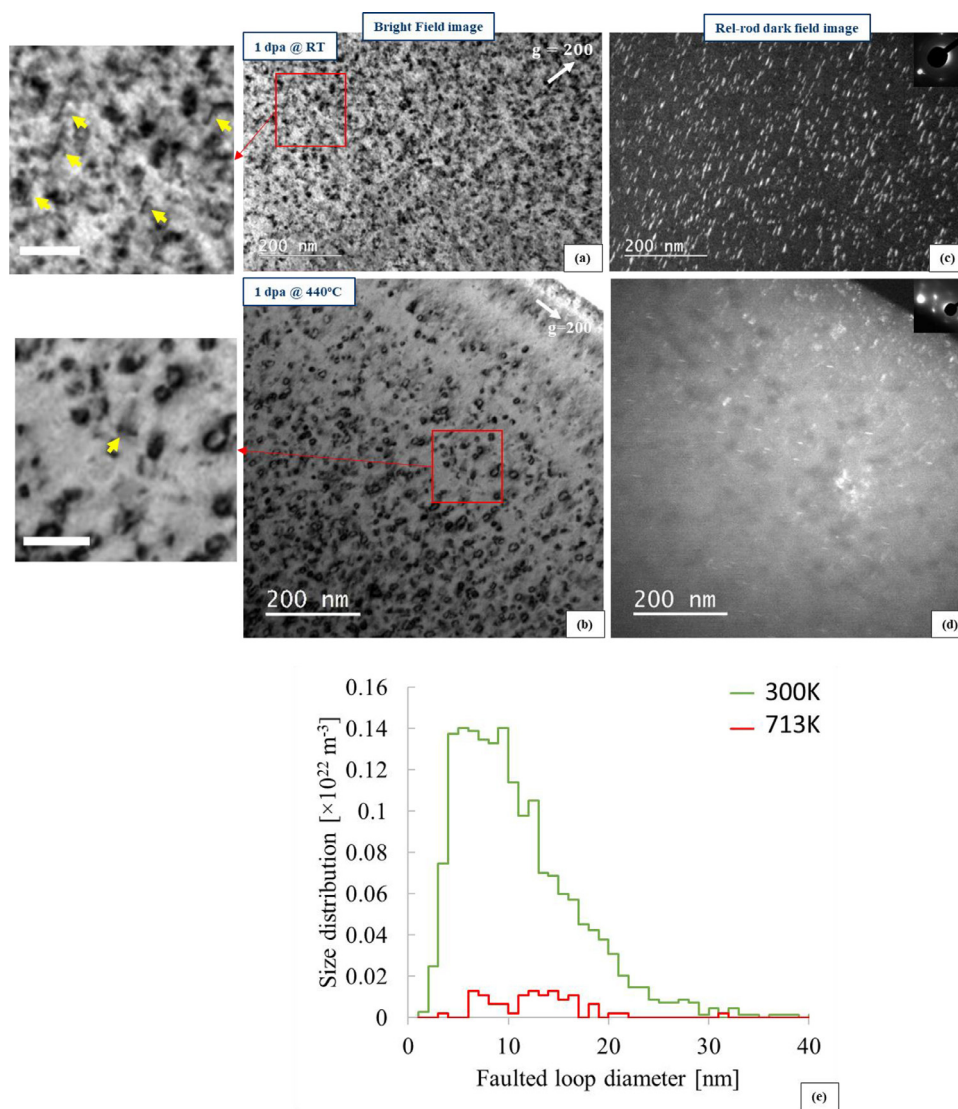
Fig. 13. (a-b) Bright field transmission electron micrograph showing 1 dpa irradiated microstructure of 21Cr32Ni model alloy at 300K and 713K. Some of the {111} type faulted loops are highlighted with the arrows in the high magnification images shown on the left [scale bar=50 nm] (c-d) Corresponding rel-rod dark field TEM images showing the faulted loops, (e) Faulted loop size distribution measured from the rel-rod dark field TEM micrographs given in (c-d).

tion made during in situ irradiation that loops can react and coalesce, forming larger loops. This provides a mechanism whereby a distinctly larger average diameter loop population can be created.

Finally, the formation of new phases as a result of irradiation can be verified using in situ diffraction analysis, as new precipitates or separate phases have a different crystal structure and thus a different diffraction pattern from the matrix. We now discuss other general; observations and their causes.

4.1. Defect alignment observed in 21Cr32Ni model alloy and alloy 800H

Irradiation of 21Cr32Ni model alloy and alloy 800H between 50K and 300K both resulted in defect alignment whereby defects were self-ordered in the <100> direction at the doses above 0.5 dpa. Similar defect cluster alignment was previously reported in both fcc and bcc metals under neutron, ion, and electron irradiation [31-34]. The temperature range at which defect alignment detected is likely to be material dependent. For example, systematic high-voltage electron microscopy (HVEM) studies of fcc Cu and Ni [31] showed that defect cluster alignment occurs only at temperatures above 170K and 380K, respectively. In our study, defect alignment was observed at irradiation temperature as low as 50K and 300K. Also, the defect alignment direction depends on the crystal structure. For fcc metals, the defect clusters have been reported to align in the <100> direction which is consistent with our observations. The Burgers vector was found to be consistent with [1̄10]. In contrast in bcc metals, the defect cluster alignment was found to be in the <110> direction with a Burgers vector of ½<111> [35]. Topbasi et al. reported defect cluster alignment during in-situ irradiation of ferritic Fe-9Cr model alloy to 10 dpa at temperatures in between 50K-573K [35]. The formation of the aligned defect structures was attributed by the authors to the minimization of high elastic strain energy which might be created by the formation of high defect density during irradiation. From our observations during in situ irradiation is clear that such an alignment is an athermal process, i.e., one that does not require atomic diffusion or long-range motion of defect clusters.

To study the stability of the aligned defect structure at higher temperatures, an annealing experiment was performed on an 800H sample. For this purpose, the sample was first irradiated to 1 dpa at room temperature to form the ordered defect structure and then

annealed at increasing temperatures for 15 minutes for each at intervals of 373K up to 773K. Fig. 12 shows the TEM images recorded before and after the annealing of alloy 800H for each temperature. The experiment shows that once the ordered dislocation structure is formed, it remains stable, at least up to 773K. Also, the corresponding diffraction patterns showed no changes. However, the overall contrast increased, possibly indicating that some small defect clusters migrate and are absorbed by larger defect structures.

4.2. Dose and temperature dependence of defect size and density in 21Cr32Ni model alloy

The defect evolution in the 21Cr32Ni model alloy with irradiation dose and temperature can be well understood in light of the data shown in Fig. 4. First, because the defect size distribution at 50K remains constant throughout the irradiation (with an average defect cluster diameter of ~2.5 ± 0.05 nm), defect migration did not influence the steady-state defect cluster size distribution. This is true even though there is some evidence of cluster migration under ion irradiation at 50K. During in-situ irradiation at 50K, the stable defects quickly reach their final size and their density increased to saturation at about ~0.1 dpa, above which defects appear and disappear at the same rate.

During irradiation at 300K, the average defect cluster diameter increased slightly compared to what was observed at 50K due to presence of relatively larger defect clusters. However, the density of these larger clusters was low compared to that of smaller defect clusters, so that the overall defect cluster size distribution did not change significantly. On the other hand, the saturation defect density decreased by a factor of ~3 following an increase in irradiation temperature from 50K to 300K. This suggests that although increased defect mobility at the higher temperature caused some defect clusters to grow, most of the small, invisible defect clusters (<2 nm) are annihilated within the microstructure either by enhanced recombination or increase in the rate of absorption at foil surface at earlier doses which would limit their growth.

As seen in Fig. 4, the average defect diameter at 713K gradually increases with dose with no indication of saturation. The corresponding defect number density initially builds up with dose up to ~0.1 dpa due to the formation of small defect clusters. Further irradiation to ~0.5 dpa causes defect clusters to grow and to form small dislocation loops. At above ~0.5 dpa, small resolvable dislocation loops grow further with the absorption of small invisible defects. Adjacent loops can coalesce with each other to form larger dislocation loops and thus reduce the corresponding defect cluster density. The faster loop growth at 713K than at 300K likely occurs because of the increase in defect mobility at the higher irradiation temperature. It is important to note that the increase in defect mobility can also result in more defect loss to foil surface. This is true if the foil surface sink strength is higher than that of the other sinks within the microstructure. However, as defect concentration increases in the foil, the sink strength in the microstructure increases so that more defects are eventually absorbed by defect clusters.

4.3. Faulted loop behavior in 21Cr32Ni model alloy

In-situ experiments performed at 300K and 713K showed that resolvable dislocation loops in 21Cr32Ni model alloy become visible at doses above ~0.5 dpa. Most of the detected loops at 300K have a {111}-type habit plane and are thus faulted in nature, whereas at 713K, both {111}- and {110}-type loops were observed, which indicates that the faulted loops are unfaulted at the higher irradiation temperature. For this purpose, the rel-rod dark field technique was used to quantify and to compare faulted loops in the model alloy. For this purpose, a two-beam condition was used

with a g=<311> reflection near the [110] zone axis. The rel-rod streaks formed due to the {111}-type faulted loops were then centered and selected with the objective aperture to form rel-rod dark-field TEM images in which faulted loops are seen as edge-on.

Fig. 13(a-b) show the BF TEM images, while Fig. 13(c-e) show the corresponding rel-rod dark-field images recorded and measured size distributions after 1 dpa at 300K and 713K with the settings above. The rel-rod diffraction patterns did not show any rel-rod streaks during irradiation at 50K, suggesting that either faulted loops do not form, or their number is very low at this cryogenic temperature. Note that Fig. 13(c-d) show only one of the four variants of the {111} faulted loops. Therefore, the number of faulted loops counted in these images were multiplied by four to obtain the faulted loop number densities. Some of the {111}-type faulted loops imaged as edge-on in BF TEM images are highlighted with the yellow arrows in the high magnification images given on the left.

The average faulted loop diameters at 1 dpa irradiated microstructure are calculated to be 10.9 ± 1.8 nm and 12.6 ± 1.3 nm for 300K and 713K experiments, respectively. This indicates that the faulted loop size in 21Cr32Ni model alloy does not change significantly with irradiation temperature between 300K-713K. However, the faulted loop number density decreases as the irradiation temperature increases, as seen in Fig. 13(c-e). The number densities of the faulted loops after 1 dpa are calculated as $(1.8 \pm 0.4) \times 10^{22}$ m^{-3} and $(0.1 \pm 0.03) \times 10^{22}$ m^{-3} for the 300K and 713K irradiations, respectively, corresponding to a reduction of an order of magnitude. If the overall defect concentration at 1 dpa previously calculated in Fig. 4 is considered, the faulted loops at 300K constitute ~40 % of the overall defect population, as opposed to only ~13% of the overall defect population at 713K. This reduction likely results from the unfaulting of the faulted loops as a result of the interaction with nearby dislocations or loops making them invisible to the rel-rod technique which is consistent with the results of previous heavy-ion irradiation performed on 21Cr32Ni alloys where unfaulting was observed during in-situ irradiation as a result of nearby dislocation glide [17,19]. The observation of many {110} type loops at 713K is also indirect evidence of loop unfaulting since {110} type perfect loops are often observed in fcc metals as a result of unfaulting of irradiation-induced faulted loops [1,36].

4.4. The defect size and density in 21Cr32Ni in comparison with commercial alloy 800H

Fig. 11 shows that the defect number density and the average defect diameter in 21Cr32Ni model alloy at 300K are similar to those determined in alloy 800H. This is also true for 713K irradiation up to 0.1 dpa where small defect clusters having diameter of ~2-3 nm initially form, and their densities quickly increase with dose at a similar rate in both 21Cr32Ni model and alloy 800H. However, further irradiation of 21Cr32Ni model alloy to ~1 dpa at 713K cause defect clusters to grow into dislocation loops which then coalesce with each other to form larger loops, consequently reducing the corresponding defect number density. In contrast, further irradiation of the alloy 800H at 713K to ~1 dpa caused some small defect clusters to grow only a little with dose and form small dislocation loops, and the number density of defects gradually increased with dose in the microstructure.

The presence of small defect clusters with higher density in alloy 800H than in 21Cr32Ni model alloy at 713K suggests that the minor alloying elements in alloy 800H bind and trap mobile point defects, thus preventing their migration towards defect clusters, and limiting defect cluster growth. To explore this hypothesis further, the total number of point defects associated with both defect clusters and dislocation loops in the model alloy and alloy 800H were calculated and compared. In this analysis, small defect clus-
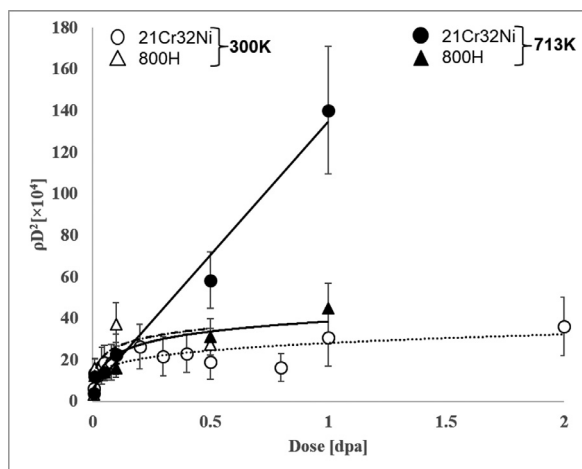
Fig. 14. Calculated number of point defects associated with the imaged defects formed in 21Cr32Ni model alloy and alloy 800H versus dose for irradiations at 300K and 713K.

ters were assumed to be small dislocation loops having an average diameter of $\bar{D}$ with a total area that is proportional to $\sim \bar{D}^2$. The total number of point defects then becomes proportional to $\sim \rho \bar{D}^2$ where ρ is the loop density which is plotted in Fig. 14. The figure shows the calculated $\rho \bar{D}^2$ values with respect to dose as a function of temperature for both alloys.

Fig. 14 shows that the total number of point defects in defect clusters and loops in the 21Cr32Ni model alloy and alloy 800H quickly increases with dose and saturates after irradiation to ~0.1 dpa at 300K. In contrast, at 713K, the number of point defects associated with defect clusters and loops increases with dose only in 21Cr32Ni model alloy. This indicates that more point defects can arrive and be absorbed by defect clusters and loops at elevated doses in 21Cr32Ni model alloy than alloy 800H during the high temperature irradiation, causing defects to grow with a faster rate. For the case of alloy 800H, however, point defects are likely to be trapped by the alloying elements, thus reducing point defect migration and leading a suppression of the number of point defects absorbed at defect clusters at 713K.

5. Summary and Conclusion

The low dose (< 2 dpa) radiation damage induced evolution of the microstructure in 21Cr32Ni model alloy was investigated with a series of in-situ 1 MeV Kr^{++} ion irradiation experiments conducted at irradiation temperatures between 50K and 713K. The model alloy microstructure was compared with the irradiated microstructure of an analogous commercial alloy 800H irradiated under similar irradiation conditions. For both alloys, the dose-dependent defect cluster size distribution, and the defect cluster density were obtained as a function of temperature. Performing the experiment in-situ allowed us to discern some of the mechanisms of early radiation damage formation.

The main findings are as follows:

Initial defect formation and migration

TEM visible defect clusters (1-2 nm in diameter) start to appear at quite low doses, i.e., ~0.005 dpa. The threshold dose at which visible defect clusters appeared did not change with irradiation temperature in the temperature range between 50K-713K. Regardless of the irradiation temperature, visible defects were not mobile during irradiation.

Defect accumulation and growth

Above the threshold dose the overall defect concentration gradually increased with increasing dose and saturated at ~0.1 dpa. After this dose a dynamic equilibrium was established whereby defects were constantly created and destroyed, while the defect density remained constant. These observations are valid for both 21Cr32Ni and 800H alloys. At above 0.1 dpa, defects grew into dislocation loops in 21Cr32Ni model alloy. This growth was more pronounced as the irradiation temperature increased. In contrast no significant defect growth was observed in alloy 800H during irradiation. The mode of loop growth in 21Cr32Ni model alloy was temperature dependent: during irradiation at 300K, loop growth occurred by the accretion of the small invisible defect clusters, while at 713K, loop growth was driven both by the absorption of small invisible defect clusters and by loop coalescence directly observed in the microscope.

Radiation-induced defect alignment

With increasing dose, visible defect clusters formed aligned defect structures along the $<100>$ direction. This occurred at irradiation temperatures as low as 50K with the Burgers vector of these clusters consistent with [$\bar{1}10$]. In-situ annealing experiments showed that these aligned defect structures remain stable up to 773K, while absorbing small defect clusters.

Faulted dislocation loop evolution

At doses above 0.5 dpa faulted dislocation loops formed in 21Cr32Ni model alloy during irradiations conducted between RT and 713K. Increasing irradiation temperature did not change the average diameter of the faulted loops, but it increased the rate of loop unfaulting which rendered these loops invisible. The unfaulting process which occurs by loop interaction with network dislocations was also observed in-situ.

Comparison of the two alloys

Microstructure development under irradiation is similar in many ways for 800H and 21Cr32Ni. The threshold dose for visible defects was the same as was the saturation dose, as well as the average defect size and number density at irradiation temperatures below 713 K. Above that temperature clusters grow and develop into dislocation loops in 21Cr32Ni but not in 800H. The likely explanation is that the alloying elements in 800H trapped the point defects and caused the defect clusters not to grow into loops.

Declaration of Competing Interest

The authors declare that they have no known competing financial interests or personal relationships that could have appeared to influence the work reported in this paper.

References

[1] G.S. Was, J. Mater. Res. 30 (2015) 1158–1182.
[2] K.L. Murty, I. Charit, J. Nucl. Mater. 383 (2008) 189–195.
[3] U.S. DOE NERAC and the Generation IV International Forum "A Technology Roadmap for Generation IV Nuclear Energy Systems", 2002.
[4] G.S. Was, T.R. Allen, J.T. Busby, J. Gan, D. Damcott, D. Carter, M. Atzmon, E.A. Kenik, J. Nucl. Mater. 270 (1999) 96–114.
[5] G.S. Was, J.T. Busby, T.R. Allen, E.A. Kenik, A. Jensson, S.M. Bruemmer, J. Gan, A.D. Edwards, P.M. Scott, P.L. Andreson, J. Nucl. Mater. 300 (2002) 198–216.
[6] K.J. Stephenson, G.S. Was, J. Nucl. Mater. 456 (2015) 85–98.
[7] F.A. Garner, W.G. Wolfer, J. Nucl. Mater. 102 (1981) 143–150.
[8] F.A. Garner, W.G. Wolfer, J. Nucl. Mater. 122 (1984) 201–206.
[9] D.J. Edwards, E.P. Simonen, S.M. Bruemmer, J. Nucl. Mater. 317 (2003) 13–31.
[10] B.H. Sencer, G. Was, M. Sagisaka, Y. Isobe, G.M. Bond, F.A. Garner, J. Nucl. Mater. 323 (2003) 18–28.
[11] A. Etienne, J. Nucl. Mater. 400 (2010) 56–63.
[12] S. Jublot, X. Li, M.L. Lescoat, F. Fortuna, A. Gentils, J. Nucl. Mater. 480 (2016) 436–446.
[13] H. Jin, E. Ko, S. Lim, J. Kwon, C. Shin, J. Nucl. Mater. 493 (2017) 239–245.
[14] J. Gupta, J. Hure, B. Tanguy, L. Laffont, M.C. Lafont, E. Andrieu, J. Nucl. Mater. 501 (2018) 45–58.
[15] Z. Jiao, J. Michalicka, G.S. Was, J. Nucl. Mater. 501 (2018) 312–318.
[16] T. Kimoto, K. Furuya, H. Shiraishi, J. Nucl. Mater. 179-181 (1991) 507–510.
[17] M. Desormeaux, B. Rouxel, A.T. Motta, M. Kirk, C. Bisor, Y. de Carlan, A. Legris, J. Nucl. Mater. 475 (2016) 156–167.
[18] S. Xu, Z. Yao, M.L. Jenkins, J. Nucl. Mater. 386-388 (2009) 161–164.
[19] M. Ayanoglu, A.T. Motta, J. Nucl. Mater. 510 (2018) 297–311.
[20] J. Gan, J.I. Cole, T.R. Allen, S. Shutthanandan, S. Thevuthasan, J. Nucl. Mater. 351 (2006) 223–227.
[21] C.J. Ulmer, A.T. Motta, J. Nucl. Mater. 498 (2018) 458–467.
[22] L. Tan, J.T. Busby, H.J.M. Chichester, K. Sridharan, T.R. Allen, J. Nucl. Mater. 437 (2013) 70–74.
[23] A.P. Druzhkov, D.A. Perminov, A.E. Davletshin, J. Nucl. Mater. 384 (2009) 56–60.
[24] A.P. Druzhkov, V.L. Arbuzov, D.A. Perminov, J. Nucl. Mater. 341 (2005) 153–163.
[25] P. Jung, H. Klein, J. Nucl. Mater. 179-181 (1991) 503–506.
[26] F.A. Garner, A.S. Kumar, in: Radiation-Induced Changes in Microstructure: 13th International Symposium (Part I), 955, ASTM, STP, 1987, pp. 289–314.
[27] J.F. Ziegler, M.D. Ziegler, J.P. Biersack, Nucl. Instrum. Methods, Phys. Res. Sect. B, Beam Interact. Mater. Atoms 268 (2010) 1818–1823.
[28] M.A. Kirk, M.L. Jenkins, Characterization of Radiation Damage by Transmission Electron Microscopy', IOP Publishing Ltd., 2001.
[29] C.A. Schneider, W.S. Rasband, K.W. Eliceiri, NIH Image to ImageJ: 25 years of image analysis, Nature Methods 9 (2012) 671–675.
[30] C. Topbasi, A.T. Motta, M.A. Kirk, J. Nucl. Mater. 425 (2012) 48–53.
[31] A. Seeger, N.Y. Jin, F. Phillipp, M. Zaiser, Ultramicroscopy 39 (1991) 342–354.
[32] S.J. Zinkle, L.K. Snead, J. Nucl. Mater. 225 (1995) 123–131.
[33] W. Jäger, H. Trinkaus, J. Nucl. Mater. 205 (1993) 394–410.
[34] M. Zaiser, W. Frank, A. Seeger, Solid State. Phenomena Vol. 23-24, (1992) 221–236.
[35] S. Hayakawa, Y. Hayashu, T. Okita, M. Itakura, K. Suzuki, Y. Kuriyama, Nucl. Mater. Energy 9 (2016) 581–586.
[36] A. Kubota, W.G. Wolfer, Mater. Sci. Eng. A 400-401 (2005) 362–365.
[37] C. Topbasi, D. Kaoumi, A.T. Motta, M.A. Kirk, J. Nucl. Mater. 466 (2015) 179–186.